ARTICLES
PUBLISHED ONLINE: 1 NOVEMBER 2009 | DOI: 10.1038/NMAT2567
nature materials

Nanostructured arrays of semiconducting octahedral molecular sieves by pulsed-laser deposition

Anais E. Espinal[1], Lichun Zhang[2], Chun-Hu Chen[3], Aimee Morey[3], Yuefeng Nie[4], Laura Espinal[1], Barrett O. Wells[4], Raymond Joesten[3], Mark Aindow[1,2] and Steven L. Suib[1,2,3]*

Cryptomelane-type manganese oxide (OMS-2) has been widely used to explore the semiconducting and catalytic properties of molecular sieves with mixed-valent frameworks. Selective synthesis of patterned thin films of OMS-2 with hierarchical nanostructures and oriented crystals is challenging owing to difficulties in preserving the mixed valence, porosity and crystalline phase. Here, we report that pulsed-laser ablation of OMS-2 in an oxygen-rich medium produces a three-dimensional nanostructured array of parallel and inclined OMS-2 fibres on bare substrates of (001) single-crystal strontium titanate. Both parallel and inclined OMS-2 fibres elongate along the $[001]_{OMS\text{-}2}$ direction. The parallel fibres interact strongly with the substrate and grow epitaxially along $\langle 110\rangle_{STO}$ with lattice misfits of less than 4%, whereas the inclined fibres are oriented with (301) parallel to the substrate surface. The spontaneous orientation of the crystalline OMS-2 domains over the STO surface opens up a new avenue in lattice-engineered synthesis of multilayer materials.

Porous materials, such as molecular sieves and zeolites, show exceptionally useful properties in catalysis, petroleum refining, gas cleansing, separation, membranes and chemical sensors[1–3], owing to their stable frameworks composed of micro, meso and macroporous tunnels that selectively allow access to specific ions, molecules and clusters. Controlled fabrication of highly oriented three-dimensional (3D) films in which functional crystal surfaces are more accessible further enhances and optimizes their already novel functionalities[2] as in membranes[3,4], photocatalysts[5] and sensors[5].

Conventional methods for preparing oriented films involve lengthy liquid-phase chemistry approaches or hydrothermal treatments that require the use of templates or seeds to direct crystallization[3–5]. Cancrinite[6] and chabazite[7] have been reported to grow epitaxially on sodalite using hydrothermal treatment for the formation of the zeolite film. Thin films of other zeolites[8–10] and molecular sieves[11,12] have been prepared by combining pulsed-laser deposition (PLD) for the seeding step with hydrothermal treatment for the formation of the film. Amorphous titanium oxide has been grown in a nanocolumnar array by PLD, but such a structure required a polystyrene colloidal monolayer as a template[5]. Other procedures require indirect methods of deposition that involve *in situ* decomposition of target compounds through laser ablation that induce deposition of the actual desired material. Thin films of $La_{0.5}Sr_{0.5}FeO_3$ fibres perpendicular to strontium titanate ($SrTiO_3$, STO) substrates have been prepared by PLD through decomposition of a $La_{0.5}Sr_{0.5}FeO_3$ target[13], although both the target and substrate materials have the same dense perovskite structure. The development of procedures that produce 3D structures of porous materials by means of self-assembly (seedless) and direct deposition from a target of the corresponding material would facilitate scale-up and improve cost-effectiveness.

Cryptomelane-type manganese oxide is the most extensively studied of the manganese oxide octahedral molecular sieves (OMS) owing to its excellent catalytic activity and semiconductor properties[14]. The oxide is designated OMS-2 and has a composition of $KMn_7^{4+}Mn^{3+}O_{16}$, where the charge imbalance on the octahedral framework owing to reduction of Mn^{4+} to Mn^{3+} is balanced by K^+ in one dimensional tunnels along the *c* axis. This mixed valence in the structure is what gives OMS-2 materials their good semiconducting properties[15]. A myriad of synthetic methods and morphologies have been reported for OMS-2 (ref. 16). Although oriented films of OMS-2 would be highly desirable for numerous applications, preparation of such films has proven to be very challenging owing to the difficulty in maintaining the mixed valence, porosity and crystal phase of the cryptomelane structure.

To address the need for the development of highly oriented thin films of OMS-2 with a 3D nanostructured architecture, we have used a method that involves deposition of OMS-2 onto single-crystal (001)STO by means of self-assembly using direct laser ablation of a target made of OMS-2 powder material. STO has the cubic perovskite structure ($a = 0.391$ nm) and is an excellent substrate for the epitaxial growth of high-temperature superconductors and many other oxide-based thin films[17]. PLD was used in this work owing to its ability to produce thin films of a wide variety of complex oxides in which the stoichiometry of the target is replicated in the film. This technique uses a high-energy ultraviolet laser, with laser pulses as short as 10–15 fs, capable of ablating a thin surface layer from a target while leaving the remainder of the target virtually unheated[18]. The present work shows the direct formation of a nanostructured array of OMS-2 with an open architecture of parallel and inclined fibres, which provide more surface accessibility both for sensing applications and for the deposition of other functional materials.

In a typical experiment, a single-crystal (001)STO substrate is placed in the PLD chamber and heated at a rate of 20 °C min^{-1} up to 600 °C under a vacuum of $\sim 1 \times 10^{-6}$ torr. Then a KrF excimer laser (wavelength = 248 nm, pulselength = 20 ns) is used to ablate the OMS-2 target material using a partial pressure of oxygen of ~200 mtorr for the desired deposition time. At the end of the

[1]Institute of Materials Science, University of Connecticut, Storrs, Connecticut 06269-3136, USA, [2]Chemical, Materials & Biomolecular Engineering, University of Connecticut, Storrs, Connecticut 06269-3222, USA, [3]Chemistry Department, University of Connecticut, Storrs, Connecticut 06269-3060, USA, [4]Department of Physics, University of Connecticut, Storrs, Connecticut 06269-3046, USA. *e-mail: Steven.Suib@uconn.edu.

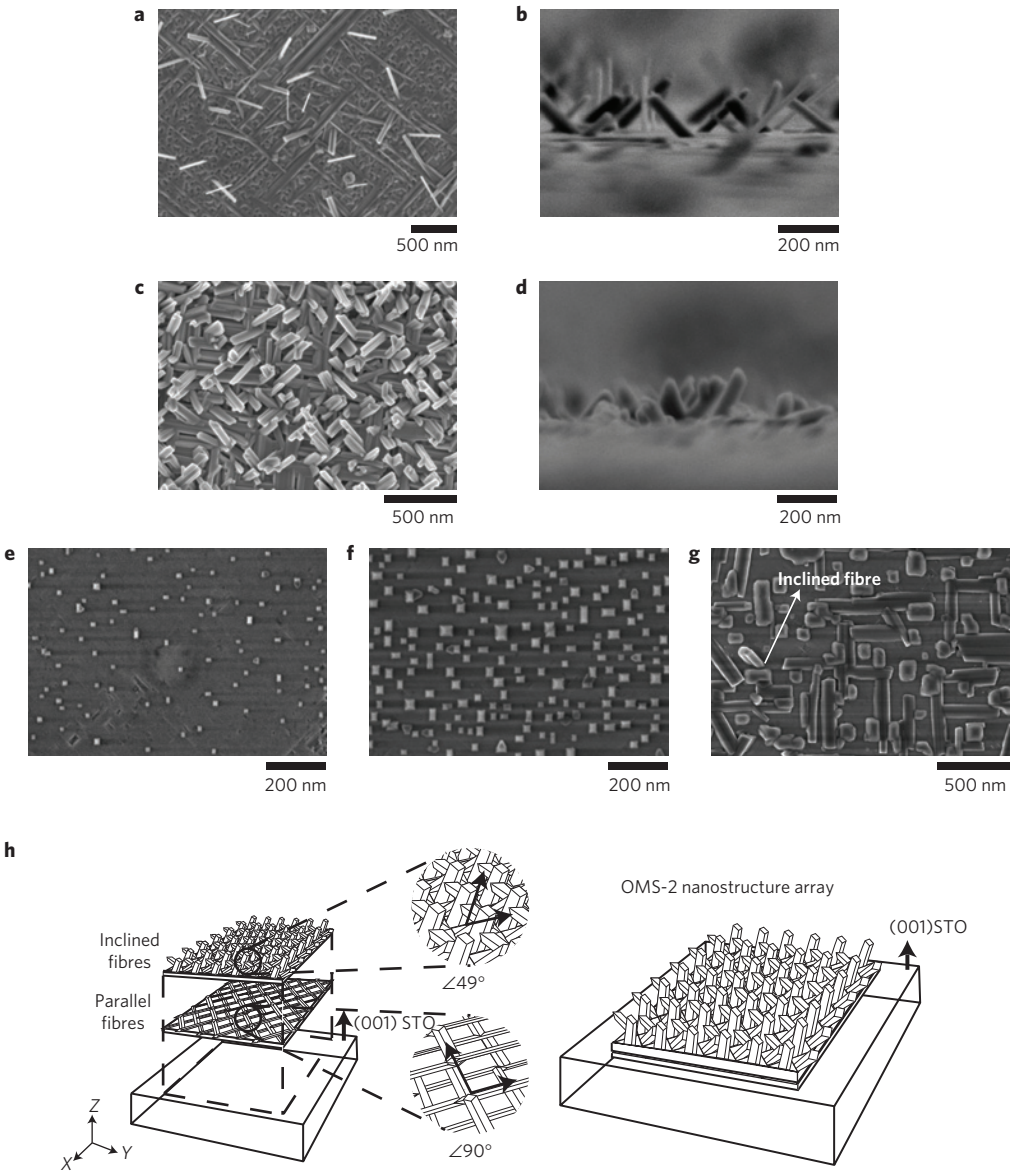

Figure 1 | Morphology and evolution of the OMS-2 nanostructured array. a–d, Secondary-electron SEM micrographs of the OMS-2 nanostructured array prepared by PLD at 600 °C using 200 mtorr partial pressure of O_2 on a single-crystal (001)STO substrate for 5 min (**a**,**b**) and for 30 min (**c**,**d**) (top and cross-sectional views in each case). **e–g**, Secondary-electron SEM images of deposits formed after 30 min showing regions at increasing distance from a mask edge giving successively smaller reductions in incident flux as compared with the film deposited without a mask in **c**,**d**. **h**, Schematic illustration of the OMS-2 nanostructured array derived from the secondary-electron SEM images. Within the array, two different fibre arrangements are observed with respect to the substrate surface: inclined fibres and parallel fibres.

deposition, the partial pressure of oxygen is increased to 300 torr and the film is then allowed to cool slowly at a rate of 2 °C min^{-1} until room temperature is reached.

The OMS-2 nanostructured arrays grown on (001)STO by PLD were observed using secondary-electron imaging in the scanning electron microscope (SEM). Planar and cross-sectional views are shown after different deposition times: 5 min (Fig. 1a,b) and 30 min (Fig. 1c,d). Figure 1a,b reveals the morphology of the nanostructured array with fibres in two distinct arrangements. The first is composed of orthogonal arrays of fibres that lie with their major axes parallel to the ⟨110⟩ directions in the STO surface (see parallel fibres in Fig. 1h), whereas the second is composed of fibres that are inclined at an angle of approximately 50° to the STO substrate surface and for which the major axes lie parallel to the ⟨100⟩ directions in the STO surface in projection (see inclined fibres in Fig. 1h). Figure 1a,b suggests that a deposition time of 5 min is not enough to obtain a dense film that would cover the substrate completely. Increasing the deposition time to 30 min greatly improves the homogeneity of the nanostructured array (see Fig. 1c,d). Both the morphology and thickness were very uniform across the substrate surface for the 30-min-deposition samples. The thickness of this film was ~200 nm and the length and thickness of the inclined fibres were approximately 200 nm and 60 nm, respectively. The OMS-2 target material also showed a fibre-like morphology but with fibre sizes varying from 20 to 60 nm in width and 200 to 500 nm in length (see Supplementary Section S1).

A further PLD experiment was carried out in which a mask was used to block the path of the plume to part of the substrate surface. At the edges of the masked regions, the effective material flux was greatly reduced; as a result, the secondary-electron SEM images obtained from such regions gave a useful insight into the evolution of the fibre arrangements. Three examples are shown

in Fig. 1e–g, which were obtained at increasing distances from the projected position of the mask edge (that is, increasing material flux from Fig. 1e–g). These images reveal a gradual development of the parallel fibre morphology from the initial nuclei, with average particle sizes and length-to-width ratios (L/W) of approximately 28 nm with $L/W = 1.2$, 42 nm with $L/W = 1.3$ and 216 nm with $L/W = 1.6$, respectively. The images also suggest that the inclined fibres nucleate directly on the STO substrate before the coalescence of the parallel fibres, although we cannot preclude the possibility that there is a thin layer of the parallel fibre deposit between the inclined fibres and the substrate. We assume that the composition of the initial nuclei is the same as that of the film and therefore such films may arise from these nuclei. A schematic representation of the arrangement for these nanostructured OMS-2 arrays is shown in Fig. 1h.

The OMS-2 powder target material and a sample of the OMS-2 nanostructured array on the (001)STO substrate were characterized by X-ray diffraction (XRD) and representative XRD patterns are shown in Fig. 2. The 2θ angles and intensities of the peaks in the pattern from the OMS-2 target material (Fig. 2, bottom) are in good agreement with the standard pattern for the pure tetragonal cryptomelane phase (JCPDS 29-1020), although a regression analysis of the data revealed that the lattice parameters were 0.4% larger ($a_0 = 0.986$ nm and $c_0 = 0.286$ nm, compared with $a_0 = 0.982$ nm and $c_0 = 0.285$ nm for the standard). All of the peaks in the corresponding XRD pattern from the thickest nanostructured fibre array (Fig. 2, top) could also be identified as arising from the cryptomelane phase of MnO_2. The regression analysis gave similar values for the lattice parameters ($a_0 = 0.988$ nm and $c_0 = 0.286$ nm), demonstrating that the structure and stoichiometry of the target material had been preserved. The main difference between the XRD patterns obtained from the nanostructured array and that from the target is the absence of certain diffraction peaks. Thus, in Fig. 2, top, all of the *hkl* peaks for which $l \neq 0$ are absent, with the exception of the 301 peak. This gives clear evidence for strong crystallographic texture in the deposit, although it was not possible to reconcile the systematic absences with any single orientation relationship with respect to the substrate.

Cross-sectional transmission electron microscopy (TEM) analysis was carried out to investigate the relationship between the unique morphology revealed in the secondary-electron SEM images of the OMS-2 nanostructured array and the crystallographic texture suggested by the XRD pattern. To preserve all of the fibre features in the array, the cross-sectional TEM samples were prepared by focused ion beam (FIB) milling with the section plane parallel to (110)STO (see Supplementary Section S2). A bright-field TEM image obtained from one such specimen is shown in Fig. 3a. Three types of fibre can be identified, as shown schematically in Fig. 3b: (1) parallel fibres A, with their major axes parallel to $[1\bar{1}0]$, which lies in the plane of the TEM cross-section, (2) parallel fibres B, with their major axes parallel to [110] (that is, perpendicular to fibres A) and thus appear 'end-on' in the image and (3) inclined fibres C, with major axes that lie in the plane of the cross-section but are inclined at an angle of approximately 50° with respect to the surface of the film. We note that although the fibres have well-defined characteristic aspect ratios, their cross-sections are rather irregular (see fibres B in this section).

Electron energy-loss spectroscopy (EELS) mapping with a Gatan imaging filter detector was used to reveal the distribution of the chemical species within the section. One example is shown in Fig. 3c, which is a bright-field image together with the corresponding O–Mn–Ti element map. The map was obtained by multivariate histogram analyses based on multiple spatially aligned images of EELS elemental maps for O, Mn and Ti individual elements. Such maps confirm that the OMS-2/STO interface is abrupt and energy-dispersive X-ray spectrometry (EDXS) spectra

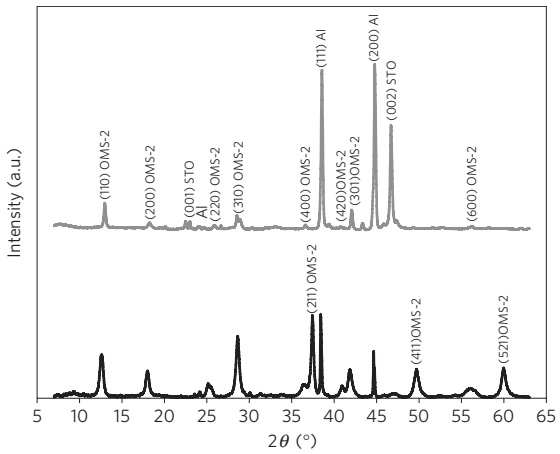

Figure 2 | Crystal structure and preferred orientation. XRD patterns of the OMS-2 powder target material (bottom) and the OMS-2 nanostructured array on single-crystal (001)STO substrate prepared by PLD at 600 °C using 200 mtorr of O_2 partial pressure for 30 min (top). The indices of reflecting planes belonging to the OMS-2 phase (JCPDS 29-1020), STO (JCPDS 35-734) and aluminium (JCPDS 4-787) are indicated. The peaks corresponding to the planes (211), (411) and (521) of the OMS-2 phase are missing in the XRD pattern of the nanostructured array suggesting that the deposit has a strong crystallographic texture with respect to the (001)STO substrate.

obtained from the fibres in this region show no evidence of interdiffusion of the substrate cations (see Fig. 3d).

The crystallographic orientation relationship between the OMS-2 fibres and the single-crystal (001)STO substrate was deduced from high-resolution TEM (HRTEM) lattice images. Two examples are shown in Fig. 3e and f, which were obtained from the interface with fibres A1 and B2 in Fig. 3a, respectively. A lattice fringe analysis reveals that these fibres have their major axes parallel to $[001]_{OMS\text{-}2}$, and that they adopt inequivalent orientation relationships with respect to the (001)STO substrate, with fibre A1 having:

$$[001]_{OMS\text{-}2} \parallel [1\bar{1}0]_{STO}, \quad [110]_{OMS\text{-}2} \parallel [110]_{STO}, \quad (110)_{OMS\text{-}2} \parallel (001)_{STO} \qquad \text{(OR-1)}$$

whereas fibre B2 has:

$$[001]_{OMS\text{-}2} \parallel [110]_{STO}, \quad [010]_{OMS\text{-}2} \parallel [1\bar{1}0]_{STO}, \quad (100)_{OMS\text{-}2} \parallel (001)_{STO} \qquad \text{(OR-2)}$$

From a series of such images it was found that the two sets of parallel fibres (A and B) show a mixture of different orientation relationships with (OR-1) and (OR-2) being the most common. All of the other orientation relationships observed also had $[001]_{OMS\text{-}2} \parallel \langle 110 \rangle_{STO}$. We note that this multiplicity of orientation relationships leads to the formation of grain boundaries between adjacent fibres with different orientation relationships, or even within a single fibre (for example, Fig. 3g and h, respectively). It is thought that this latter effect may be related to the rather irregular cross-sections shown by the fibres.

To understand the formation of these multiple orientation relationships, it is useful to consider the atomic arrangements for the various interfacial configurations. The $[1\bar{1}0]_{STO}$ and $[110]_{STO}$ projections of the structures on either side of the interface for (OR-1) are shown in Fig. 4a. In the first projection, the misfit, δ, between the primitive lattice translation vectors $0.5[110]_{STO}$ and

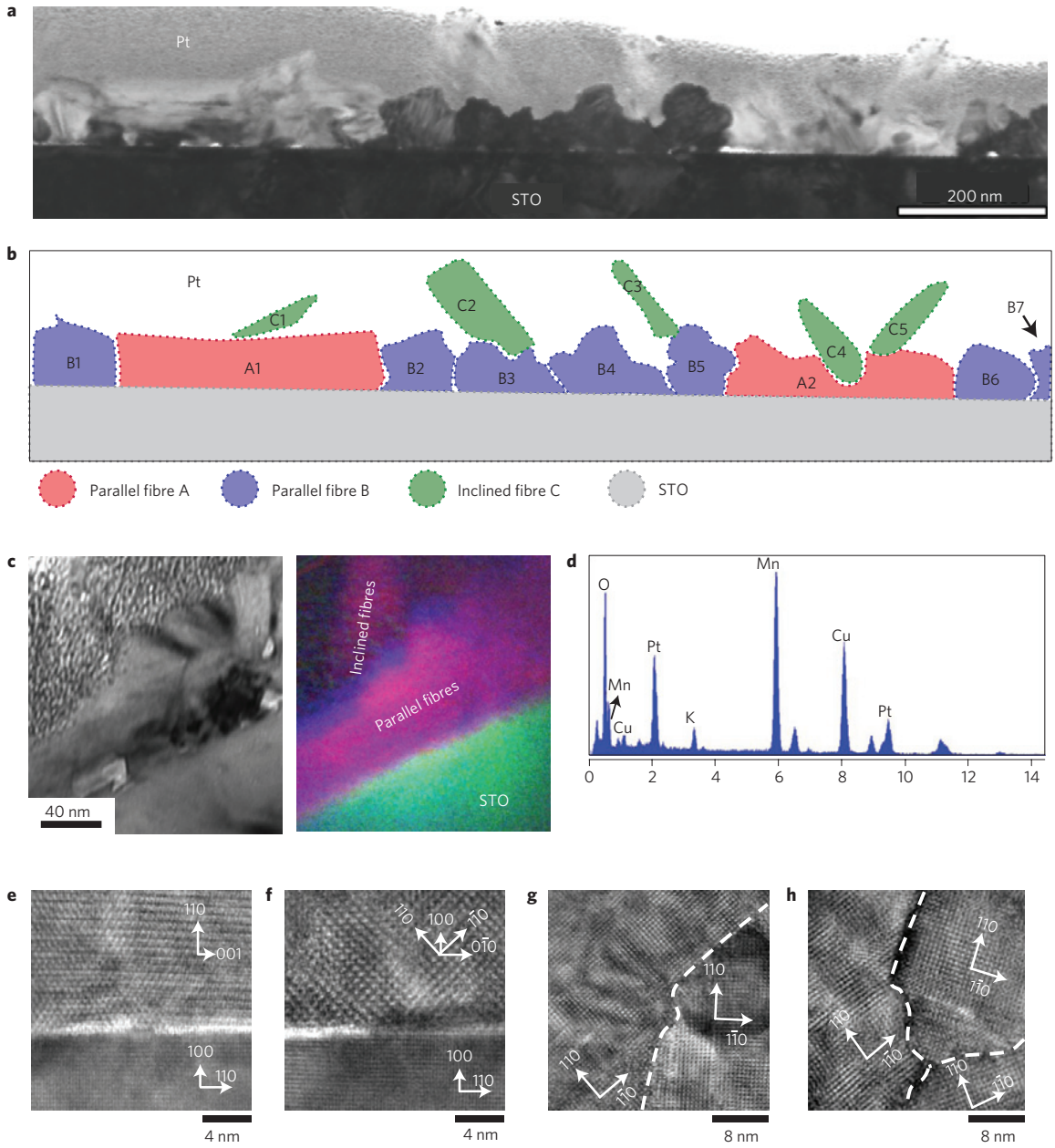

Figure 3 | Microstructure of the OMS-2 nanostructured array. a, Cross-sectional TEM image of the OMS-2 nanostructured array deposited on a (001)STO substrate by PLD. The TEM specimen was FIB-cut along $[110]_{STO}$. **b**, Schematic showing the three groups of fibres (A, B and C) of Fig. 3a. **c**, TEM image with a corresponding colour-coded O–Mn–Ti elemental map (blue for O, red for Mn and green for Ti) constructed from energy-filtering data. **d**, EDXS elemental analysis of one inclined fibre. **e**–**h**, HRTEM images of the parallel fibre A1/STO interface (**e**), parallel fibre B2/STO interface (**f**), boundary between parallel fibres B2/B3 (**g**) and within fibre B5 (**h**).

$[001]_{OMS\text{-}2}$ is only 3.4%. No such simple low-δ correspondence exists in the orthogonal direction, but one can identify a supercell in which $2.5[1\bar{1}0]_{STO}$ matches $[1\bar{1}0]_{OMS\text{-}2}$ with $\delta = 1.1\%$. Figure 4b contains the corresponding $[1\bar{1}0]_{STO}$ and $[110]_{STO}$ projections of an A fibre with (OR-2). Here again, δ along the major axis of the fibre is 3.4%, but in the orthogonal direction a supercell is required to obtain a modest value of δ; in this case, the supercell involves $3.5[1\bar{1}0]_{STO}$ matching $2[0\bar{1}0]_{OMS\text{-}2}$, giving $\delta = 2.1\%$. Thus, the most likely explanation for the parallel OMS-2 fibres adopting (OR-1) and (OR-2) with respect to the STO substrate is the existence of low-misfit supercells in the atomic interfacial structure at these orientations. Similar arguments can be applied to the other orientation relationships observed experimentally, although these are less common than (OR-1) and (OR-2).

Most of the features in the XRD pattern can be accounted for on the basis of the orientation relationships adopted by these parallel fibres. As the X-ray diffractometer samples those planes oriented parallel to the specimen surface, and the common feature of the orientation relationships for the parallel fibres is $[001]_{OMS\text{-}2} \parallel \langle 110 \rangle_{STO}$, one would expect all of the *hkl* peaks for which $l \neq 0$ to be absent, as observed experimentally (with the exception of 301, which is discussed below). Moreover, as the preferred orientation relationships are (OR-1) and (OR-2), one would expect an enhancement in the 110 and 200 peaks, respectively, over that for a randomly oriented powder sample (such as the target material); here again, this effect is observed experimentally in the XRD pattern (Fig. 2, top, and Supplementary Table S1).

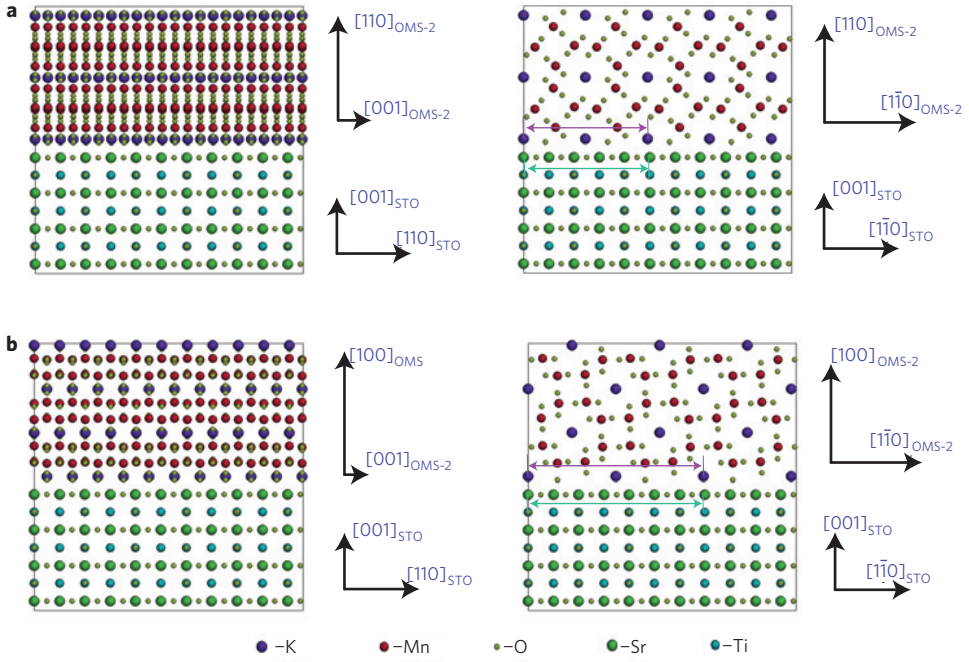

Figure 4 | Heteroepitaxial growth. Atomic arrangements at the interface for the two most common orientation relationships observed for the parallel fibres in the OMS-2 nanostructured array on (001)STO. **a**, OR-1: $[001]_{OMS\text{-}2} \parallel [110]_{STO}$, $[110]_{OMS\text{-}2} \parallel [110]_{STO}$ and $[110]_{OMS\text{-}2} \parallel [001]_{STO}$. **b**, OR-2:$[001]_{OMS\text{-}2} \parallel [110]_{STO}$, $[010]_{OMS\text{-}2} \parallel [110]_{STO}$ and $[100]_{OMS\text{-}2} \parallel [001]_{STO}$.

As the 301 peaks are not consistent with the orientation relationships for the parallel fibres, they presumably arise from the inclined fibres. This is consistent with the inclination of these fibres to the STO surface (Figs 1b,d and 3a) and was confirmed using selected-area diffraction on plan-view TEM specimens, as shown in Supplementary Section S4. Thus, it seems that these inclined fibres show two crystallographically equivalent variants of the same orientation relationship:

$$[10\bar{3}]_{OMS\text{-}2} \parallel [100]_{STO}, \qquad [010]_{OMS\text{-}2} \parallel [010]_{STO}$$
$$(301)_{OMS\text{-}2} \parallel (001)_{STO} \qquad \text{(OR-3)}$$

In this case, there is no simple low-δ correspondence in the interface, and the values of δ are large even if supercells are considered. Thus, if the inclined fibres do nucleate directly on the STO substrate, then the most likely interfacial arrangement would be a supercell in which $3[100]_{STO}$ matches $[10\bar{3}]_{OMS\text{-}2}$ with $\delta = 11.7\%$, and $3[010]_{STO}$ matches $[010]_{OMS\text{-}2}$ with $\delta = -15.5\%$ (see Supplementary Section S5). Although these values are rather higher than one would usually expect for the growth of an epitaxial deposit, they could be sustained over small areas as secondary nuclei, and there is some suggestion of such nuclei in images such as Fig. 1f,g. Such secondary nuclei could be over-grown by the fibres that develop from the lower misfit primary nuclei during lateral growth of the deposit. If, however, this does not occur, then the development of protrusions by unconstrained growth from these secondary nuclei would naturally lead to the development of the inclined fibre morphology observed experimentally because the growth rate for OMS-2 is highest along [001]. The arrangement of both parallel and inclined fibres in the OMS-2 nanostructured array along the [001] direction (see Fig. 1h) coincides with the one-dimensional tunnel of OMS-2. The growth of OMS-2 material in this direction is characteristic of this material[19–21].

Control of the temperature and background pressure of oxygen during the PLD process were key parameters to maintain the cryptomelane phase in the thin films. Generally, deposition of thin films at high temperatures is desired for epitaxial growth owing to increased mobility of the atoms at the surface. The deposition temperature used here was 600 °C to prevent thermal decomposition of the OMS-2, which takes place at higher temperatures[22] (see Supplementary Section S6). Similarly, the use of an oxidizing environment may have helped in the formation and stabilization of the cryptomelane phase, as reported for other oxide thin films prepared by PLD (ref. 18). The use of low partial oxygen pressure led to the reduction of MnO_2 to Mn_2O_3 or Mn_3O_4 thin films on other substrates[23].

The epitaxial growth of OMS-2 reported here is in contrast to previous unsuccessful attempts to deposit zeolites directly by means of PLD. This may be related to the use of single crystals as substrates and to the colour of the materials. OMS-2 is black, whereas zeolites are white. If the visible-light absorption characteristics were replicated for the appropriate ultraviolet wavelength then OMS-2 would absorb more of the laser pulse energy than a zeolite, resulting in more energetic species in the plume and a greater propensity to form ordered crystalline deposits on arrival at the substrate.

We demonstrated the heteroepitaxial growth of OMS-2 on a (001)STO substrate using PLD. The direct ablation of an OMS-2 target material by a focused pulsed-laser beam in an oxygen-rich environment produced a thin film composed of fibres arranged in a unique 3D nanostructured pattern, which had the crystalline structure, mixed valence and chemical composition of the target material. The highly oriented array of OMS-2 fibres was grown on STO without using extra templates or seeds to direct the crystal orientation and growth. Both parallel and inclined fibres were elongated along the $[001]_{OMS\text{-}2}$ direction, and the main orientation relationship in the crystals within the fibres parallel to the STO surface was found to be $[001]_{OMS\text{-}2} \parallel [110]_{STO}$ with a lattice mismatch of less than 4%. The degree of orientational control reported here holds great promise for new lattice-engineered functional materials. Tunable orientation of the crystal domains is expected to be obtained by the selection of different substrates. Even though the OMS-2 nanostructured array obtained

is not a single crystal, these porous thin films may be very useful as substrates for the manufacture of ultrahigh-surface-area composites for multifunctional device applications in the field of catalysis, energy storage and photovoltaics. This work also suggests a pathway towards the formation of similar nanostructures with other complex porous oxides such as zeolites.

Methods

OMS-2 target material preparation. OMS-2 powder material was prepared by a sol–gel combustion method[22]. The procedure involved the preparation of solution A by mixing 10 mmol of potassium nitrate and 4.6 mmol of manganese nitrate in 50 ml of deionized and distilled water. Solution B was prepared by dissolving glycerol, used as crosslinking agent, in 30 ml of deionized and distilled water. The molar ratio of salts to glycerol was set to 1:2. Solution B was slowly added to solution A while stirring at room temperature until a homogeneous clear solution (solution C) was formed. Evaporation of solution C was carried out on a hot plate until the water was completely removed. The recovered dry gel was heated to 250 °C for 6 h and later calcined at 600 °C for 6 h. The yield of this preparation is about 4 g of OMS-2 powder. OMS-2 target material was prepared by pressing about 2 g of OMS-2 powder into a cylindrical pellet of 2.5 cm × 0.3 cm using a mechanical cold press. The pressure used was about 70 MPa and the holding time was 6 min, which assured the pellet was dense enough for the ablation process.

PLD experiments. PLD experiments were carried out using pellets of the OMS-2 material as targets and single-crystal (001)STO as substrates (MTI Corporation) with dimensions of 10 mm × 10 mm × 0.5 mm. Before deposition, the substrates were cleaned using ethanol in an ultrasonication bath for 20 min and handled with care. Bare substrates of (001)STO were subsequently glued on the heater of the PLD system with silver paste to enhance the thermal conductivity during the heating process. The PLD chamber was evacuated to a base vacuum pressure of $\sim 1 \times 10^{-6}$ torr before deposition. The temperature of the substrate was controlled and monitored throughout the processes of heating, deposition and cooling. The partial pressure of oxygen during deposition was kept at 200 mtorr, using an oxygen flow of 10 sccm; whereas during the cooling period, the oxygen partial pressure was increased to 300 torr. The conditions of the laser were 22 kV, repetition rate 4 Hz and 200 J, operating at a fluence of 11 J mm^{-2}. This laser passed through the ultraviolet-grade fused-silica window and into a vacuum chamber with an angle of incidence of 45° relative to the target surface. The distance between the substrate, which was held upside down inside the chamber, and the target was ∼9.5 cm. Both the substrate and the target were rotated (at 10 and 13 r.p.m., respectively) to avoid local heating during the laser ablation.

Characterization. The resulting OMS-2 nanostructured arrays were characterized using XRD, SEM, TEM, EELS and EDXS. Lattice parameters, average particle sizes and orientation relationships were determined to understand the formation of this unique nanostructured array. XRD measurements were carried out using a Scintag XDS 2000 diffractometer with a Cu Kα X-ray source using a current and voltage of 40.0 mA and −45.0 kV, respectively. The films were attached to an aluminium holder and XRD patterns were collected in step-scan mode with a step size of 0.02° and a dwell time of 10 s. SEM studies were carried out using a Zeiss DSM 982 Gemini field-emission scanning electron microscope with a Schottky emitter operating at 2.0 kV with a beam current of 1.0 mA. The thicknesses of the films were determined by imaging the cross-section of the samples with field-emission scanning electron microscopy. The average particle size and the lattice parameters were calculated using the ImageJ[24] and Unitcell[25] programs, respectively. The cross-sectional TEM specimen was prepared with a FEI Strata 400 Dual Beam FIB and later examined with a JEOL 2010 FasTEM operating at 200 kV. This latter instrument is equipped with a high-resolution objective lens pole-piece (spherical aberration coefficient $Cs = 0.5$ mm) giving a point-to-point resolution of <0.19 nm in phase-contrast images. Chemical microanalysis was carried out using an EDAX Phoenix atmospheric thin-window EDXS. In addition, the elemental maps of the specimen were collected using a Gatan imaging filter detector. The image filtering was carried out using the O K-, Mn L- and Ti L-edges at 532, 540 and 456 eV, respectively. The structural model of interfacial features observed in the HRTEM images was established and analysed using CrystalKit[26] software.

Received 22 July 2009; accepted 6 October 2009; published online 1 November 2009

References

1. Corma, A. From microporous to mesoporous molecular sieve materials and their use in catalysis. *Chem. Rev.* **97,** 2373–2419 (1997).
2. Davis, M. E. Ordered porous materials for emerging applications. *Nature* **417,** 813–821 (2002).
3. Lai, Z. *et al.* Microstructural optimization of a zeolite membrane for organic vapour separation. *Science* **300,** 456–460 (2003).
4. Dong, J., Lin, Y. S., Kanezashi, M. & Tang, Z. Microporous inorganic membranes for high temperature hydrogen purification. *J. Appl. Phys.* **104,** 121301 (2008).
5. Li, Y., Sasaki, T., Shimizu, Y. & Koshizaki, N. Hexagonal-close-packed, hierarchical amorphous TiO_2 nanocolumn arrays: Transferability, enhanced photocatalytic activity, and superamphiphilicity without ultraviolet irradiation. *J. Am. Chem. Soc.* **130,** 14755–14762 (2008).
6. Okubo, T. *et al.* Heteroepitaxial growth of a zeolite. *Angew. Chem. Int. Ed.* **40,** 1069–1071 (2001).
7. Wakihara, T., Yamakita, S., Iezumi, K. & Okubo, T. Heteroepitaxial growth of a zeolite film with a patterned surface-texture. *J. Am. Chem. Soc.* **125,** 12388–12389 (2003).
8. Xiong, C., Coutinho, D. & Balkus, K. J. Jr Fabrication of hollow spheres composed of nanosized ZSM-5 crystals via laser ablation. *Micropor. Mesopor. Mater.* **86,** 14–22 (2005).
9. Muñoz, T. Jr & Balkus, K. J. Preparation of oriented zeolite UTD-1 membranes via pulsed laser ablation. *J. Am. Chem. Soc.* **121,** 139–146 (1999).
10. Pisklak, T. J. & Balkus, K. J. Preparation and characterization of UTD-12/ZSM-48 thin films via pulsed-laser deposition. *Micropor. Mesopor. Mater.* **81,** 125–134 (2005).
11. Washmon-Kriel, L. & Balkus, K. J. Preparation and characterization of oriented MAPO-39 membranes. *Micropor. Mesopor. Mater.* **38,** 107–121 (2000).
12. Balkus, K. J. Jr & Scott, A. S. Zeolite coatings on three-dimensional objects via laser ablation. *Chem. Mater.* **11,** 189–191 (1999).
13. Mohaddes-Ardabili, L. *et al.* Self-assembled single-crystal ferromagnetic iron nanowires formed by decomposition. *Nature Mater.* **3,** 533–538 (2004).
14. Suib, S. L. Porous manganese oxide octahedral molecular sieves and octahedral layered materials. *Acc. Chem. Res.* **41,** 479–487 (2008).
15. Tian, Z. R. *et al.* Manganese oxide mesoporous structures: Mixed-valent semiconducting catalysts. *Science* **276,** 926–930 (1997).
16. Suib, S. L. Structure, porosity, and redox in porous manganese oxide octahedral layer and molecular sieve materials. *J. Mater. Chem.* **18,** 1623–1631 (2008).
17. Vrejoiu, I., Alexe, M., Hesse, D. & Goesele, U. Functional perovskites—from epitaxial films to nanostructured arrays. *Adv. Funct. Mater.* **18,** 3892–3906 (2008).
18. Chrisey, D. B. & Hubler, G. K. *Pulsed Laser Deposition of Thin Films* (Wiley, 1994).
19. Li, W.-N. *et al.* Hydrothermal synthesis of structure- and shape-controlled manganese oxide octahedral molecular sieve nanomaterials. *Adv. Funct. Mater.* **16,** 1247–1253 (2006).
20. Yuan, J., Li, W.-N., Gomez, S. & Suib, S. L. Shape-controlled synthesis of manganese oxide octahedral molecular sieve three-dimensional nanostructures. *J. Am. Chem. Soc.* **127,** 14184–14185 (2005).
21. Yuan, J. *et al.* Superwetting nanowire membranes for selective absorption. *Nature Nanotech.* **3,** 332–336 (2008).
22. Liu, J., Makwana, V., Cai, J., Suib, S. L. & Aindow, M. Effects of alkali metal and ammonium cation templates on nanofibrous cryptomelane-type manganese oxide octahedral molecular sieves (OMS-2). *J. Phys. Chem. B* **107,** 9185–9194 (2003).
23. Isber, S. *et al.* Study of manganese oxide thin films grown by pulsed laser deposition. *Thin Solid Films* **517,** 1592–1595 (2009).
24. Abràmoff, M. D., Magalhães, P. J. & Ram, S. J. Image processing with ImageJ. *Biophoton. Int.* **11,** 36–41 (2004).
25. Holland, T. J. B. & Redfern, S. A. T. UNITCELL: A nonlinear least-squares program for cell-parameter refinement implementing regression and deletion diagnostics. *J. Appl. Crystallogr.* **30,** 84 (1997).
26. Kilaas, R. & O'Keefe, M. A. in *Computer Simulation of Electron Microscope Diffraction and Images* (eds Krakow, E. W. & O'Keefe, M. A.) (TMS, 1989).

Acknowledgements

We thank the US Department of Energy (DOE), Geosciences and Biosciences Division, Office of Basic Energy Sciences, Office of Science and NSF award number DMR-0907197, for financial support. We would like to thank R. Ristau for preparing cross-section samples on the FIB-TEM and J. Romanow for helping acquiring secondary-electron SEM images. X. Shen and F. Galasso were very helpful with suggestions and encouragement.

Author contributions

A.E.E., C.-H.C. and S.L.S conceived and designed the experiments. A.E.E., Y.N. and B.O.W. carried out PLD experiments. A.E.E collected crystal structure data and SEM images and analysed them along with L.E., R.J. and S.L.S. L.Z. and M.A. collected the TEM data and analysed the orientation relationships. A.M. prepared the OMS-2 target material. A.E.E., L.E, L.Z., M.A. and S.L.S. co-wrote the paper. All authors discussed the results and commented on the manuscript.

Additional information

The authors declare no competing financial interests. Supplementary information accompanies this paper on www.nature.com/naturematerials. Reprints and permissions information is available online at http://npg.nature.com/reprintsandpermissions. Correspondence and requests for materials should be addressed to S.L.S.